Submillimetre continuum images of the NGC 2024 star-forming ridge.

Anja E. Visser, John S. Richer, Claire J. Chandler, Rachael Padman[1]

ABSTRACT

We present 450-μm and 800-μm images, made with the James Clerk Maxwell Telescope, of the NGC 2024 molecular ridge. The seven previously known compact cores, FIR1-7, have been detected, and FIR5 has been resolved into a compact object and an associated extended source to the east. The estimated masses of the dense cores vary between 1.6 and 5.1 $M_\odot$ per $14''$ beam, assuming a dust temperature of 30 K and a dust opacity of $\kappa_{800\mu m} = 0.002\ m^2\ kg^{-1}$. A spectral index map made from the 450-μm and 800-μm images shows spatial variations, with the spectral index, α ($F_\nu \propto \nu^\alpha$), being systematically lower towards the dense cores. We interpret this as evidence for a lower value of the frequency dependence of the dust opacity, β, towards the denser cores relative to the surrounding molecular material. This may indicate grain growth is occurring in the cores, prior to planetesimal formation. By comparing the high resolution 450-μm image with interferometer maps of the integrated CS(2–1) emission, the previously reported discrepancy between dust continuum emission and molecular line emission has been found to be very localised. Depletion and temperature variations are discussed as possible explanations.

Subject headings: circumstellar matter - stars: formation - ISM: individual: NGC 2024 - ISM: molecules

1. Introduction

NGC 2024 is part of the Orion Molecular Cloud complex at a distance of 415 pc (Anthony-Twarog 1982). It includes a dense molecular ridge coincident with an HII region towards which an infrared cluster has also been identified (Barnes et al. 1989; Lada et al. 1991). The ridge is believed to lie behind the HII region and there are indications of an interaction between the ionized gas and the dense molecular material (Gaume, Johnston & Wilson 1992). NGC 2024 harbours stars at all phases of evolution, such as B stars ionizing the HII region, young members of the

[1]Postal address: Mullard Radio Astronomy Observatory, Cavendish Laboratory, Madingley Road, Cambridge CB3 0HE, United Kingdom

infrared cluster, embedded protostars, and possibly some condensations that may yet form stars (Lada et al. 1991; Mezger et al. 1988; Chandler & Carlstrom 1996, hereafter C&C96). Because of this diversity, NGC 2024 is an ideal region to investigate the relationship between stars, protostars, condensations, and their immediate surroundings.

Of particular interest are the seven compact sources, FIR1-7, revealed by dust continuum emission from the molecular ridge. Mezger et al. (1988, 1992) discovered these sources by mapping the ridge in 1300-μm and 870-μm continuum emission and suggested that these cores are isothermal condensations about to collapse to form protostars. This suggestion has been the impulse for several detailed investigations and triggered a discussion about the true nature of these seven objects. Those investigations revealed a 2-μm source (Moore & Chandler 1989), a reflection nebula (Moore & Yamashita 1995) and a unipolar outflow (C&C96), all associated with FIR4. A highly collimated, unipolar, molecular outflow extending over several arcmin is associated with FIR5 (Sanders & Willner 1985; Richer et al. 1989, Richer, Hills & Padman 1992), and associated with FIR6 is a water maser (Genzel & Downes 1977) and a compact outflow with an extremely short dynamical age of ~ 400 yr (Richer 1990). Such findings prove that the associated millimeter sources, FIR4-6, contain embedded protostars or young stars. The evolutionary states of FIR1-3, and FIR7 have not yet been determined.

Here we present high resolution 450-μm ($\theta_{\rm beam} = 8''$) and 800-μm ($\theta_{\rm beam} = 14''$) continuum emission images of the ridge and its compact sources. These data constrain the spectral energy distributions of the embedded sources, and provide the resolution necessary for comparisons of the distribution of the dust with that of molecular line emission as shown by interferometric measurements. No molecular counterparts to the compact dust cores have been detected so far, suggesting depletion of the molecules from the gas phase, or spatial variations in the excitation conditions (Schulz et al. 1991; Mauersberger et al. 1992; Wilson, Mehringer & Dickel 1995; Wiesemeyer et al. 1997; C&C96).

2. Observations and Data Analysis

The continuum observations of the NGC 2024 molecular ridge were made at wavelengths of 450 μm and 800 μm, using the James Clerk Maxwell Telescope on Mauna Kea, Hawaii. The 800-μm (375 GHz) and 450 μm (667 GHz) continuum data were obtained in 1992 October and 1993 February respectively, using the UKT14 single-element bolometer, cooled to 0.36 K (Duncan et al. 1990). Maps were made 'on-the-fly', with the telescope scanning continuously in azimuth whilst the secondary mirror chopped at a frequency of 7.8125 Hz, using a chop throw of $40''$ in azimuth. Several scans obtained at different elevations then make up an 'on-the-fly' map. The final 800-μm image of NGC 2024 is composed of seven overlapping on-the-fly maps, each with cell size $4''$, and the final 450-μm image is composed of three such maps, with a cell size of $2''$.

The data were initially reduced and analysed using the software packages FIGARO and JCMTDR. After interpolating bad pixels, a baseline which was linear in time was subtracted from individual azimuth scans to correct for instrumental drifts. The data were then corrected for the atmospheric extinction, assuming that the zenith optical depth varies linearly with time between the values measured at the beginning and end of each observation. For the 800-μm maps these optical depths were obtained using diffraction-limited photometric measurements of the secondary calibrator source NGC 2071IR (Sandell 1994). The optical depths used for the atmospheric correction on the 450-μm maps were obtained by using the zenith optical depths at 1300 μm, $\tau_{1300\mu\mathrm{m}}$, measured regularly by the tipping radiometer at the Caltech Submillimeter Observatory. A ratio of $\tau_{450\mu\mathrm{m}}/\tau_{1300\mu\mathrm{m}} \approx 20$ was found from fits to photometric measurements of CRL 618 during the 5 observing nights. Absolute flux density calibration at 800-μm and 450-μm was obtained from observations of Mars and CRL 618 (Sandell 1994). The estimated systematic errors are approximately 50% at 450-μm and 15% at 800-μm; these result from fluctuations in the optical depth of the atmosphere, and from uncertainties in the coupling efficiency of the beam to the calibrators.

Dual-beam maps obtained in on-the-fly mode can be represented by a convolution of the true sky brightness with a dual-beam function, which varies slowly with time owing to source rotation. This dual-beam function is a convolution of a pair of delta functions of opposite sign separated by the chop throw, and the single beam power pattern of the antenna. The calibrated on-the-fly maps must be restored to obtain equivalent single-beam maps, co-added, and converted to equatorial coordinates. There are two different methods to do this: one is to use the traditional Emerson, Klein & Haslam (EKH) algorithm (Emerson, Klein & Haslam 1979) and the other method is to use a maximum entropy algorithm such as DBMEM (Richer 1992). We have chosen to use the maximum entropy algorithm here for the reasons given in Richer (1992), which results in *deconvolved* images.

Because of small pointing errors (typically a few arcseconds), the positions of the FIR sources in the different on-the-fly maps must be aligned before the maps can be used to create the final images. As calibration positions we used the positions of FIR2-6 from C&C96, and of FIR1 from Wilson, Mehringer & Dickel (1995). These positions are listed in Table 1. The position offsets between the on-the-fly maps and these calibration positions were found to be smaller than $4''$ in declination and $7''$ in right ascension, and were taken into account by the maximum entropy algorithm. Although the maximum entropy algorithm results in images with better resolution, the analysis of both the maximum entropy and EKH images lead to very similar results.

3. Results and Discussion

In Figs 1 and 2 we present the 450-μm and 800-μm maximum entropy images of NGC 2024. The similarity between the 870-μm image made using the IRAM telescope with an angular resolution of $\theta_{\rm beam}$ = 8″ by Mezger et al. (1992) and the 800-μm JCMT image ($\theta_{\rm beam}$ = 14″) is striking despite the difference in beam sizes. The similarity of the two images is a direct demonstration of the difference in the two mapping algorithms, DBMEM and EKH, and gives us confidence in our DBMEM images.

The cores FIR1-6 are detected at 800 μm, and enhanced continuum emission is also observed around the position of FIR7 (Fig. 2). Both this latter source as well as the cores FIR2-6 are detected clearly at 450 μm (Fig. 1). Small gaps in the coverage of the ridge exist in the 450 μm map owing to the changing parallactic angle during the observations (see the dotted lines, Fig. 1), and only emission from FIR3, 5 and 6 is *fully* covered at this wavelength although most of the emission from FIR2, 4, and 7 is also detected. The two images correlate very well in their overall structure. There is, however, a striking contrast between the 800-μm image and the 450-μm image at the location of FIR5. At 800 μm FIR5 is extended east-west, but at 450 μm FIR5 is clearly resolved into a compact source and an extended feature which seems to correspond to structure observed in CS(2–1) emission by C&C96 (see also Wiesemeyer et al. 1997). This feature east of the compact source has not previously been detected in continuum emission. Another feature seen in both 450-μm continuum emission and CS(2–1) emission, which does not appear on the 800-μm map, can be found between FIR2 and 3. The difference between the 450- and 800-μm images cannot be explained by a difference in resolution, and we conclude that the 450-μm image of NGC 2024 differs locally from the 800-μm image, suggesting small-scale, frequency-dependent structure caused by variations in optical depth, temperature, or dust properties.

To obtain the peak flux densities per beam for the FIR cores, we smoothed the deconvolved 800-μm image with a 14″ Gaussian (FWHM) and the 450-μm image with an 8″ Gaussian. The results are presented in Table 1. The rms noise (σ) measured in the smoothed 450-μm map is 2.5 Jy beam^{-1} and in the smoothed 800-μm map it is 0.87 Jy beam^{-1}. The peak flux densities obtained from the maximum entropy images are similar, but systematically lower (with an average of 1.5 σ) than those obtained from images produced using the EKH algorithm. This is a well known problem with maximum entropy reconstructions (see, e.g., Cohen 1991), but the signal-to-noise ratio of the emission from each source is high enough that the derived flux densities are affected by much less than the calibration uncertainties. The flux density integrated over the molecular ridge at 800 μm is 204$\pm$30 Jy, which agrees very well with the 225$\pm$45 Jy detected at 870 μm by Mezger et al. (1992). At 450 μm the limited sky coverage provides a lower limit to the integrated flux density of 850$\pm$425 Jy (see Fig. 1).

3.1. Submillimetre Spectral Index

To investigate possible variations of the submillimetre spectral index, α (defined by $F_\nu \propto \nu^\alpha$) across the source, a spectral index map was made using the 800-μm and 450-μm deconvolved images both smoothed to $14''$ resolution (Fig. 3). It is striking that the spectral index is lower around the FIR cores ($\alpha \sim 2.9$) compared with the surrounding molecular cloud ($\alpha \sim 3.5$), which might be explained by higher optical depth in the dense cores, lower temperatures, or variations in the dust properties. We discuss these possibilities below. A spectral index map made with the EKH images, both convolved to the same resolution, shows a similar decrease of α near the FIR cores, demonstrating that this is not an artefact of the DBMEM images.

3.1.1. Dust Optical Depth, Temperature Structure and Dust Opacity

The first explanation we consider for the low values of α found towards the FIR cores is that the dust emission is optically thick. The high resolution achieved in our deconvolved 450-μm image allows us to calculate a lower limit to the peak optical depth, τ_ν, from

$$\tau_\nu = -\ln\left(1 - \frac{F_\nu}{B_\nu(T)\Omega}\right), \qquad (1)$$

where $B_\nu(T)$ is the Planck function for temperature T and Ω is the solid angle over which the flux density F_ν has been measured. The peak emission in the 450-μm map, 1.2 Jy/arcsec^2, coincides with FIR3; the 450-μm peak emission at FIR5 and FIR6 is 0.7 Jy/arcsec^2. The optical depths corresponding to these intensities depend on the dust temperature assumed. In the literature temperatures between 19 K (Mezger et al. 1992) and 30 K (C&C96) are used. If the cores contain embedded heat sources, as might be expected in sources driving powerful outflows, dust temperatures of 19 K are likely to be underestimates and molecular line studies also point towards higher temperatures, $T_{\rm dust} \sim 30$ K (e.g., Chandler, Moore & Emerson 1992; Ho et al. 1993). The low value of 19 K comes from estimated colour temperatures (Mezger et al. 1988), and has been shown to be inconsistent with high-resolution interferometer data (C&C96). For these reasons we use a dust temperature of 30 K, and we find an optical depth at 450 μm of 0.25 for FIR3 and 0.14 for FIR5 and FIR6. In the extreme limit that we assume a temperature of 19 K, the optical depth is 0.72 for FIR3 and 0.36 for FIR5 and FIR6, which can cause a maximum change in the spectral index of 0.4 and 0.2 respectively. The typical difference in the spectral index between the ridge and the FIR cores is 0.5–0.6, and it is thus unlikely that such a difference is caused by optical depth alone.

Another possible explanation of a decrease of the spectral index towards the denser cores is that the temperature in the cores is low compared with the temperature of the surrounding material. If the dust emission is optically thin, the spectral index can be written as $\alpha = 2 + \beta + \gamma$, where γ is a Rayleigh-Jeans correction factor, and the dust opacity, κ_ν, is expressed as a power-law function of frequency at long wavelengths; $\kappa_\nu = \kappa_0(\nu/\nu_0)^\beta$. The Rayleigh-Jeans correction factor, γ, is given by

$$\gamma = 1 - \log\left(\frac{\exp(h\nu_1/kT) - 1}{\exp(h\nu_2/kT) - 1}\right) / \log\left(\frac{\nu_1}{\nu_2}\right). \tag{2}$$

for measurements of F_ν at frequencies ν_1 and ν_2. A decrease in α may indicate a decrease in β and/or γ, or an increase in optical depth. The typical difference of 0.5–0.6 could be caused by temperature differences if the denser regions are colder than the surrounding material; γ becomes more negative in these denser regions, resulting in a decrease of α (for instance if the cores were at 19 K, the surrounding material would have to be at $\gtrsim 50$ K to reproduce the observed spectral index difference). In order to investigate whether the spatial variations in α persist in material very localized around the embedded sources and in the dense cores, we have compared Fig. 1 with the 3 mm interferometer images of C&C96 (see also Chandler et al. 1996). The extended structure was removed from the 450 μm map by subtracting an image smoothed to $30''$ resolution, and the interferometer images were smoothed to $8''$ to match the 450 μm data. Flux densities integrated over $10''$ boxes were then used to calculate the spectral index. Values for α of 3.1 ± 0.2, 2.7 ± 0.2, 2.5 ± 0.2 and > 3.5 were obtained for FIR3, FIR5, FIR6 and the 450 μm peak to the east of FIR5 respectively, confirming the trends observed at $14''$ resolution. On the scales probed by the interferometer the emission is dominated by material associated directly with the embedded protostars at FIR5 and FIR6, which is likely to be at least as warm as the eastern dust ridge. This suggests that the temperature differences are not the cause of variations in α.

Neither high optical depths nor low temperatures in the cores can by themselves provide satisfying explanations for the variations in the spectral index, and we therefore propose that variations in β are the most likely cause of these variations. Typical values for α in the neighbourhood of the dense cores are 2.7–3.1, resulting in values for the frequency dependence of the dust opacity in the range 1.2–1.6, assuming a dust temperature of 30 K ($\gamma = -0.5$). In the surrounding cloud α is measured to be in the range 3.3–3.6, which results in values for β of 1.8–2.1 (assuming the same temperature). Similarly, from our comparison of the 450 μm map with the 3 mm interferometer data, we find values for β in FIR3, FIR5, FIR6 and the eastern ridge of ~ 1.6, ~ 1.1, ~ 1.0, and $\gtrsim 2$ respectively.

Several explanations have been suggested for changes in β. For example, Agladze et al. (1994) showed with a laboratory study that the dust opacity of amorphous forsterite powder has a frequency dependence different from crystalline forsterite powder. Apparently the transformation from amorphous grains to more structured particles or vica versa could result in a change in the observed β. Also, needle-like grains possess a different opacity-frequency dependence from spherical grains (see, e.g., Ossenkopf & Henning 1994), and the same is true for fluffy aggregates versus compact particles (e.g., Wright 1987). Other explanations for a changing β are a possible chemical evolution of the dust (Pollack et al. 1994), or an increase in grain size (e.g., Miyake & Nakagawa 1993; Krügel & Siebenmorgen 1994). Values for β lower than the theoretical limit for small grains ($\beta = 2$) have also been observed in T Tauri disks and have been interpreted as an indication for evolution of dust properties, possibly grain growth (Beckwith & Sargent 1991; Mannings & Emerson 1994). Particles are expected to grow through coagulation by mutual collisions in dense environments such as circumstellar disks and protostellar cores, with a coagulation timescale of $\sim 10^5$ yr at the densities observed in the FIR sources, $\sim 10^{13}$ m^{-3} (Ossenkopf 1993). However, the models of Ossenkopf & Henning (1994) predict that particle growth will affect β only if the dust grains do not have ice mantles, implying that a decrease in β may only be observed in regions of relatively high temperature, $T_{\rm dust} \gtrsim 100$ K (Draine 1985). The spatial variations in β across the NGC 2024 ridge are therefore consistent with the evolution of grain properties due to particle coagulation at high densities, provided the cores are warm enough.

We not only detect a possible evolution in β from the extended cloud emission to the dense cores, but also find a trend in the value of β between individual cores. Not only the spectral indices derived from Fig. 3 (Table 1) but also, more clearly, those obtained from the 450 μm and 3 mm interferometer data, are lower for the cores FIR5 and 6 compared with FIR3. FIR5 and 6 both contain embedded protostars and are suggested by C&C96 to be the oldest sources in the ridge, while there is no sign yet of star formation activity associated with FIR3. This indicates a correlation between β and protostellar age, again consistent with the idea of grain evolution at high densities and temperatures.

3.2. The masses of the FIR cores

If the emission is optically thin, thermal dust continuum observations can be used to estimate the masses of the cores, via $M = F_\nu D^2/\kappa_\nu B_\nu(T_{\rm dust})$, where D is the distance to NGC 2024. Different values for the dust temperature, $T_{\rm dust}$, and dust opacity, κ_ν, are used by different authors, and have resulted in quite a large range in masses calculated for these cores. The whole discussion about the true nature of the dust cores is related to the uncertainty in these two parameters. Until the turnover wavelengths of the spectral energy distributions are observed (which presumably lie in the range $300 > \lambda > 30\,\mu$m), direct dust temperatures of the cores cannot be obtained, but we use here a dust temperature $T_{\rm dust} = 30$ K for reasons mentioned in section 3.1.1. We adopt a dust opacity $\kappa_\nu = 0.01(\nu/10^{12}\,{\rm Hz})^\beta$ m^2 kg^{-1} (Hildebrand 1983) with $\beta = 1.5$ derived from the spectral index map, giving $\kappa_{800\mu{\rm m}} = 0.0023$ m^2 kg^{-1}. We note, however, that at 10^{12} Hz, values of κ_ν ranging from 0.002 to 0.02 m^2 kg^{-1} can be found in the literature (Henning et al. 1995). Using these values for the dust temperature, the dust opacity, and the 800$\,\mu$m peak flux densities of the dense cores FIR1-7, results in masses per 14$''$ beam ranging between 1.6 and 5.1 $M_\odot$ (Table 1, Column 6).

To compare our masses with those derived from millimetre interferometry imaging by C&C96, we also use their assumed value of $\beta = 1$, and obtain masses per 14$''$ beam ranging between 1.0 and 3.1 $M_\odot$. These are a factor of $\sim$2 larger than the masses derived by C&C96. The discrepancy arises from the considerable extended emission associated with the ridge to which the interferometer is not sensitive, but which we detect in our single-dish images. To assess the contribution to the mass from the extended dust ridge we have smoothed the 800-μm image with a 30$''$ Gaussian (FWHM) and subtracted it from the 14$''$ resolution image. The masses remaining in the compact structures associated with the FIR cores are then in very good agreement with the masses obtained by the Owens Valley millimetre interferometer: compare Column 7 of their Table 3 with Column 7 of our Table 1 — the mass of FIR7 is reduced from 1.8 $M_\odot$ to 0.3 $M_\odot$, which agrees much better with the 0.2 $M_\odot$ deduced by C&C96.

Mezger et al. (1992) calculated the masses of the cores assuming $T_{\rm dust} = 19\,{\rm K}$, and a dust opacity corresponding to the above parameterization for κ_ν with $\beta = 2$ ($\kappa_{800\mu{\rm m}} = 0.0014$ m^2 kg^{-1}). Using these values for $T_{\rm dust}$ and $\kappa_{800\mu{\rm m}}$ we obtain masses within 10% of those calculated by Mezger et al. for the cores FIR1, 2, 6 and 7[1]. For the more extended cores FIR3, 4 and 5 we obtain masses 50% lower, due to the fact that we used peak flux densities per beam, while Mezger et al. (1992) used flux densities integrated over Gaussian models of the sources.

3.3. Comparison of our continuum maps with molecular line studies

The seven FIR cores have been extensively studied and their true nature has been subject of debate since Mezger et al. (1988) suggested that the cores were isothermal condensations without hydrostatic embedded protostars. Observations of the molecular counterparts of these compact dust cores could in principle provide important information about the kinematics in the cores, and should settle the question about the true nature of the cores if, for instance molecular lines revealed direct spectroscopic evidence for ongoing infall. Unfortunately, molecular counterparts have not yet been detected and therefore no information is available on the kinematics of the cores.

The high resolution of our 450-μm image enables a detailed comparison of the dust emission with existing interferometric images of molecular line emission. In Fig. 4 the integrated CS(2–1) emission measured using the Owens Valley millimeter array (C&C96) is displayed in greyscale

---

[1] The mass presented for FIR7 by Mezger et al. (1992) is 9.3 $M_\odot$, but a recalculation from the flux in that paper shows it should be 3.3 $M_\odot$., suggesting a typographical error.

with 450-μm continuum contours overlayed. The CS(2–1) line is expected to trace gas with densities $\gtrsim 4 \times 10^{11}$ m^{-3} in the ridge. There is in general a good correlation between the 450-μm dust continuum and the CS(2–1) emission along the ridge. The column density can be derived from the CS(2–1) emission assuming LTE, $T_{\rm ex}$ = 40 K, τ_{21} = 1 (see C&C96), and an abundance of CS relative to H_2 of 2.5×10^{-9} (Blake et al. 1987). A typical H_2 column density in the densest CS clumps is 3–4×10^{27} m^{-2}. The H_2 column densities in the dust cores are typically 5–11×10^{27} m^{-2} assuming $T_{\rm dust}$ = 30 K and β = 1.5. The column densities derived from the dust and the CS(2–1), although uncertain, agree within a factor of 2–3. However, the densest CS clumps do not correspond to the dust condensations, and there is a clear discrepancy within $7''$ of FIR5, where there is bright continuum but no CS emission. It has been suggested that such a discrepancy might be caused by depletion of the CS molecules onto cold dust grains in the dense cold condensations (Mauersberger et al. 1992). An alternative explanation is that the temperature of the gas and dust in and near FIR5 is somewhat higher than in the surrounding ridge (Richer 1990). Emission from optically thin dust scales with the dust temperature, $T_{\rm dust}$, and emission from CS scales inversely with the gas excitation temperature, as $1/T_{\rm ex}$, if CS is optically thin, thermalized and warm enough to populate the higher energy levels. At the high densities present here (typically $\sim$ 1–2 $\times$ 10^{13} m^{-3}), $T_{\rm dust}$ and $T_{\rm ex}$ are expected to be equal, so a higher temperature would cause an increase in dust emission and a decrease in molecular line emission, resulting in a discrepancy between the observed structure in the two tracers.

Differences between dust emission and molecular line emission can also be seen in the maps of $C^{18}O$(1–0) (Wilson, Mehringer & Dickel 1995) and HCO^+(1–0) (Barnes & Crutcher 1990), but these new high resolution 450 μm data show the discrepancy to be extremely localised. In the depletion picture, the extreme localization of the discrepancy might be caused by a higher density near FIR5 with respect to the surroundings. In the high temperature scenario, the localized discrepancy might be caused by an extra heating of the dust and the gas by FIR5, which may be the oldest protostar. To be able to exclude definitely either the molecular depletion scenario or the high temperature scenario, more molecular observations are needed. Recent chemical modelling of NGC 2024 by Charnley (1997) predicts that observations of the N_2H^+ molecule should offer a test of the depletion scenario (see also Bergin & Langer 1997). Charnley shows that N_2H^+ does not deplete from the gas phase even at densities up to 2×10^{14} m^{-3}, and an almost uniform abundance across the cores is therefore expected. The high temperature scenario can be tested by observations of molecular species such as propyne, which can reveal the temperature distribution over the ridge, or of typical “hot core” molecules such as NH_2D and CH_3OH.

4. Conclusions

We have presented new 450-μm and 800-μm continuum images of the NGC 2024 molecular cloud; these are the highest resolution submillimetre images available of this region, and they clearly delineate the elongated ridge and the seven compact dust cores. The source FIR5, thought to be the driving source of the major outflow in this region, is resolved into a point source plus an extended feature to the east. A spectral index map of the ridge between 450-μm and 800-μm shows a decrease of the spectral index, α, towards the dense FIR cores. Although these variations in α might partly be explained by an increase in the optical depth or a decrease in temperature towards the cores, we demonstrate that these explanations are unlikely. Instead, we propose that the frequency dependence of the dust opacity, β, is lower in the cores, having a typical value of $\beta \approx 1.5$, as opposed to $\beta \approx 2$ in the surrounding ridge material. These spatial variations in the value of β might be due to an evolution of the properties of the grains in the FIR cores, the obvious possibility being grain growth through coagulation at the high inferred densities. We have also compared our high-resolution 450-μm images with 3-mm interferometric data and these confirm the decrease in α towards the cores compared with the surrounding cloud. We also find tentative evidence that α is lower towards the cores known to contain embedded protostars, FIR5 and 6, than towards FIR3, which shows no signs of star forming activity. If confirmed in other such objects, this might suggest that β provides a 'clock' for measuring the evolutionary state of dense dust condensations. The masses of the seven dense cores inferred from the new data vary between 1.6 and 5.1 $M_{\odot}$, using plausible assumptions about the dust temperature and opacity. After correction for the extended emission from the ridge, the masses are in good agreement with previous interferometric studies, and suggest space densities within the cores greater than 10^{13} m^{-3}. Our high-resolution 450-μm continuum map further confirms the discrepancy between optically-thin line and dust continuum emission in this region. Comparison with an interferometric CS(2–1) image of the region shows this discrepancy to be extremely localised; this is particularly evident near FIR5, where the submillimetre point source lies well away from the ridge traced by CS and dust emission, and there is no molecular counterpart to the point source FIR5 itself. A conclusive explanation for the different appearance of the line and continuum emission is still not possible: molecular depletion and temperature variations are two viable options. Whatever the cause or causes, they must be occuring on scales of less than 4,000 AU.

Acknowledgments

We would like to thank the referee for useful comments which improved this paper. AEV was supported by a PPARC studentship, an Isaac Newton studentship, and a Marie Curie Research Training Grant during the course of this work. JSR and CJC acknowledge the support of a Royal

Society Fellowship and a PPARC Advanced Fellowship respectively. The James Clerk Maxwell Telescope is operated by the Joint Astronomy Centre on behalf of the Particle Physics and Astronomy Research Council of the United Kingdom, the Netherlands Organisation for Scientific Research, and the National Research Council of Canada.

REFERENCES

Anthony-Twarog, B.J. 1982, AJ, 87, 1213

Agladze, N.I., Sievers, A.J., Jones, S.A., Burlitch, J.M., Beckwith, S.V.W., 1994, Nat, 372, 243

Barnes, P.J., Crutcher, R.M., 1990, ApJ, 351, 176

Barnes, P.J., Crutcher, R.M., Bieging, J.H., Storey, J.W.V., Willner, S.P., 1989, ApJ, 342, 883

Beckwith, S.V.W., Sargent, A.I., 1991, ApJ, 381, 250

Bergin, E.A., Langer, W.D., 1997, ApJ, 486, 316

Blake, G.A., Sutton, E.C., Masson, C.R., Phillips, T.G., 1987, ApJ, 315, 621

Chandler, C.J., Carlstrom, J.E., 1996, ApJ, 466, 338 (C&C96)

Chandler, C.J., Carlstrom, J.E., Richer, J.S., Visser, A.E., Padman, R., 1996, in Kress, M.E., Tielens, A.G.G.M., Pendleton, Y.J., eds, From Stardust to Planetesimals: Contributed Papers, NASA CP-3343, p 139

Chandler, C.J., Moore, T.J.T., Emerson, J.P., 1992, MNRAS, 256, 369

Charnley, S.B., 1997, MNRAS, 291, 455

Cohen, J.G., 1991, in Grandy Jr W.T., and Schick, L.H., eds, Maximum Entropy and Bayesian Methods, Kluwer, Dordrecht, p 59

Draine, B.T., 1985, in Black, D.C., Matthews, M.S., eds, Protostars and Planets II, Univ. Arizona Press, Tucson, p 621

Duncan, W.D., Robson, E.I., Ade, P.A.R., Griffin, M.J. & Sandell, G., 1990, MNRAS, 243, 126

Emerson, D.T., Klein, U., Haslam, C.G.T., 1979, A&A, 76, 92

Gaume, R.A., Johnston, K.J., Wilson, T.L., 1992, ApJ, 388, 489

Genzel, R., Downes, D., 1977, A&AS, 30, 145

Hildebrand, R.H., 1983, QJRAS, 24, 267

Henning, Th., Michel, B., Stognienko, R., 1995, Plant. Space Sci., 43, 1333

Ho, P.T.P., Peng, Y.-L., Torrelles, J.M., Gómez, J.F., Rodríguez, L.F., Cantó, J., 1993, ApJ, 408, 565

Krügel, E., Siebenmorgen, R., 1994, A&A, 288, 929

Lada, E.A., DePoy, D.L., Evans, N.J., Gatley, I., 1991, ApJ, 371, 171

Mannings, V., Emerson, J.P., 1994, MNRAS, 267, 361

Mauersberger, R., Wilson, T.L., Mezger, P.G., Gaume, R., Johnston, K.J., 1992, A&A, 256, 640

Mezger, P.G., Chini, R., Kreysa, E., Wink, J.E., Salter, C.J., 1988, A&A, 191, 44

Mezger, P.G., Sievers, A.W., Haslam, C.G.T., Kreysa, E., Lemke, R. Mauersberger, R., Wilson, T.L., 1992, A&A, 256, 631

Miyake, K., Nakagawa, Y., 1993, ICARUS, 106, 20

Moore, T.J.T., Chandler, C.J., 1989, MNRAS, 241, 19P

Moore, T.J.T., Yamashita, T., 1995, ApJ, 440, 722

Ossenkopf, V., 1993, A&A, 280, 617

Ossenkopf, V., Henning, Th., 1994, A&A, 291, 943

Pollack, J.B., Hollenbach, D., Beckwith, S., Simonelli, D.P., Roush, T., Fong, W., 1994, ApJ, 421, 615

Richer, J.S., 1990, MNRAS, 245, 24P

Richer, J.S., 1992, MNRAS, 254, 165

Richer, J.S., Hills, R.E., Padman, R., Russell, A.P.G., 1989, MNRAS, 241, 231

Richer, J.S., Hills, R.E., Padman, R., 1992, MNRAS, 254, 525

Sandell, G., 1994, MNRAS, 271, 75

Sanders, D.B., Willner, S.P., 1985, ApJ, 293, L39

Schulz, A., Güsten, R., Zylka, R., Serabyn, E., 1991, A&A, 246, 570

Wiesemeyer, H., Güsten, R., Wink, J.E., Yorke, H.W., 1997, A&A, 320, 287

Wilson, T.L., Mehringer, D.M., Dickel, H.R., 1995, A&A, 303, 840

Wright, E.L., 1987, ApJ, 320, 818

Table 1. Positions[a] fluxes, masses and spectral indices[b] of the FIR cores in NGC 2024.

Source	R.A. (1950)	Dec. (1950)	Peak F_ν		M[c]	M[d]	α
			450 μm	800 μm			
	(h m s)	(° ′ ″)	Jy/8″beam	Jy/14″beam	($M_\odot$/14″beam)	($M_\odot$/14″beam)	
FIR1	05 39 09.90	-01 55 11.0	···	4.2	1.6	0.4	
FIR2	05 39 10.85	-01 55 26.7	31	6.8	2.6	0.6	
FIR3	05 39 11.45	-01 55 49.2	51	11.1	4.2	1.4	3.1
FIR4	05 39 12.49	-01 56 10.1	>31	6.7	2.5	0.8	
FIR5	05 39 12.67	-01 57 03.3	44	13.4	5.1	1.6	2.8
FIR6	05 39 13.57	-01 57 27.1	29	8.7	3.3	0.7	3.0
FIR7	05 39 13.6	-01 57 43	25	4.7	1.8	0.3	

[a]Positions of FIR2-6 are from C&C96, and the positions of FIR1 and FIR7 are from Wilson, Mehringer & Dickel (1995).

[b]The spectral indices are from the spectral index map, Fig. 3.

[c]Masses of the FIR cores calculated from the 800-μm image using $\beta = 1.5$ and $T_{\rm dust} = 30$ K.

[d]Masses of the FIR cores calculated after subtracting the extended emission associated with the ridge, assuming $\beta = 1$ and $T_{\rm dust} = 30$ K, for comparison with the interferometer results of C&C96.

Figure captions

Fig. 1. The 450-μm continuum image of NGC 2024 made with DBMEM. The dotted lines indicate the borders of the three azimuth-elevation maps from which this image was made. Contours are at 2, 6, 10, 14, 18, 24, 30, and 36 times the 1σ level of level 17 mJy/arcsec^2. The positions are as quoted in Table 1.

Fig. 2. The 800-μm continuum image of NGC 2024 made with DBMEM. Contours are at 2, 5, 8, 12, 15, 20, and 25 times the 1σ level of 3.5 mJy/arcsec^2. The positions are from Table 1.

Fig 3. Spectral index map made from the 450-μm and 800-μm continuum images smoothed to the same resolution. Regions were blanked in both images if the intensity was less than twice the mean rms noise in either image. The contours are from the 450-μm continuum map 2, 6, 10, 14, 18, 24, 30, 36, and 42 times the 1σ level of 17 mJy/arcsec^2.

Fig. 4. Integrated CS(2–1) emission from C&C96 in greyscale overlaid by the 450-μm continuum contours from Fig. 1.

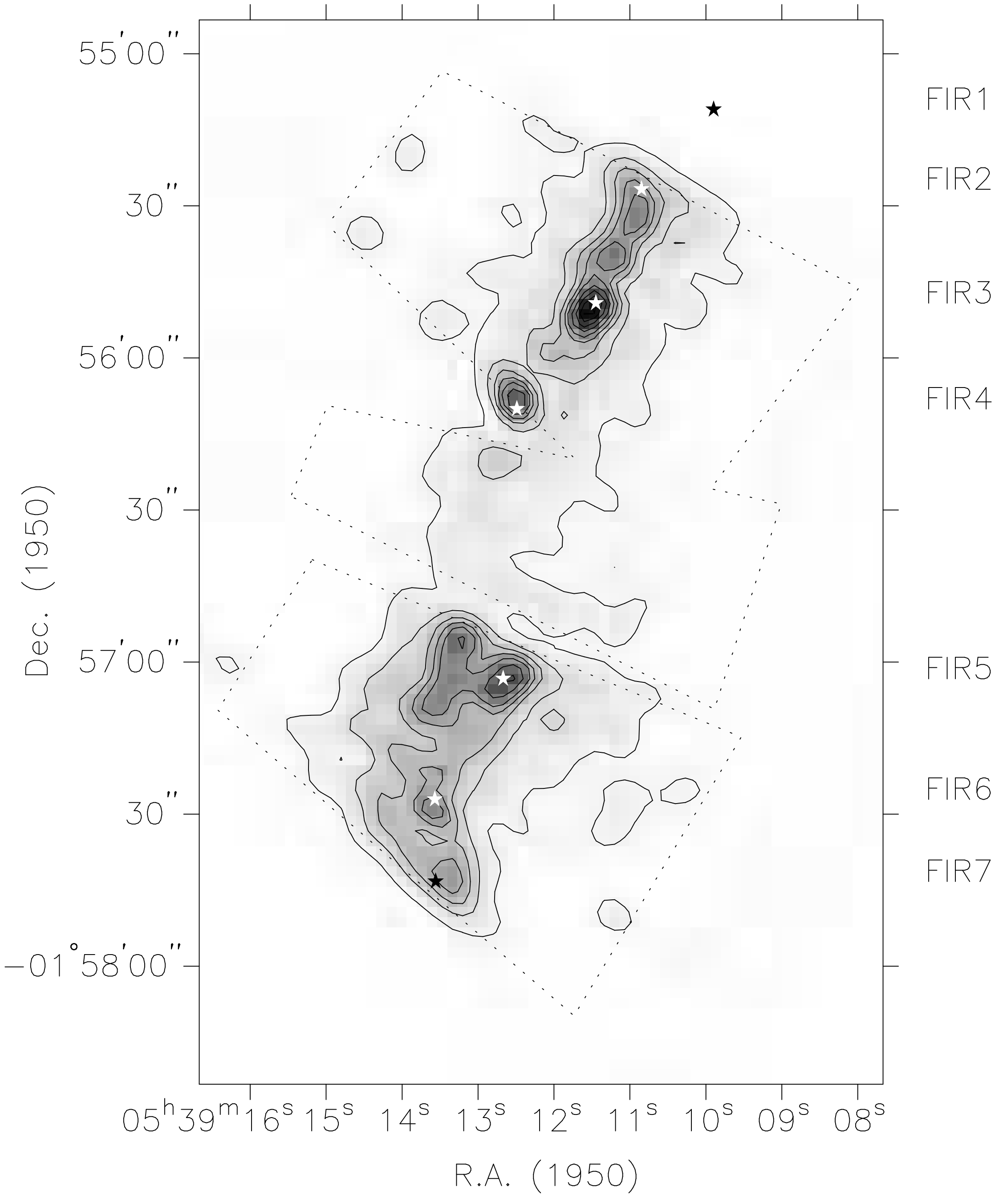
55′00″
30″
56′00″
30″
57′00″
30″
−01°58′00″
Dec. (1950)
05h39m16s 15s 14s 13s 12s 11s 10s 09s 08s
R.A. (1950)
FIR1
FIR2
FIR3
FIR4
FIR5
FIR6
FIR7

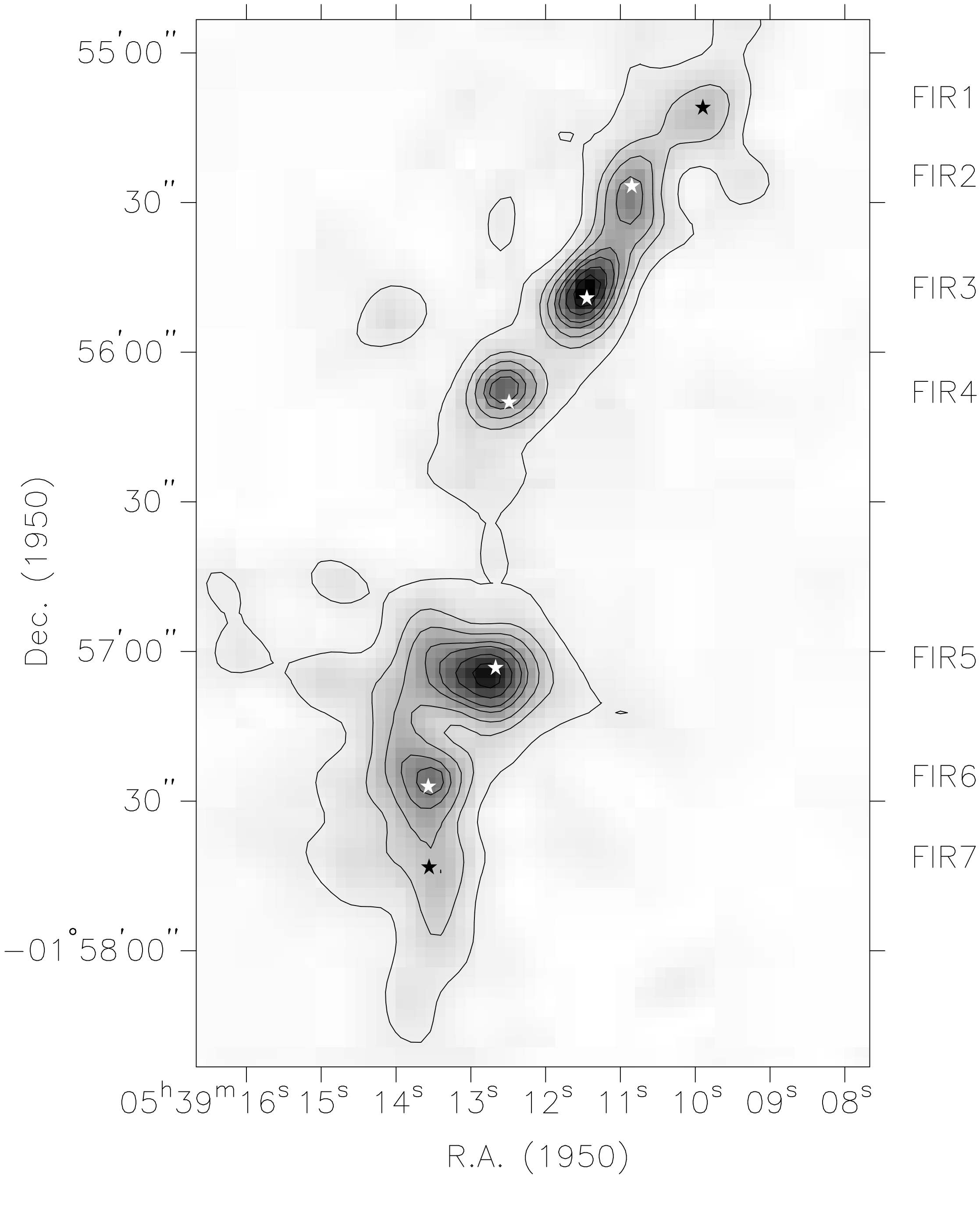
55′00″
30″
56′00″
30″
57′00″
30″
−01°58′00″
Dec. (1950)
FIR1
FIR2
FIR3
FIR4
FIR5
FIR6
FIR7
05h39m16s 15s 14s 13s 12s 11s 10s 09s 08s
R.A. (1950)

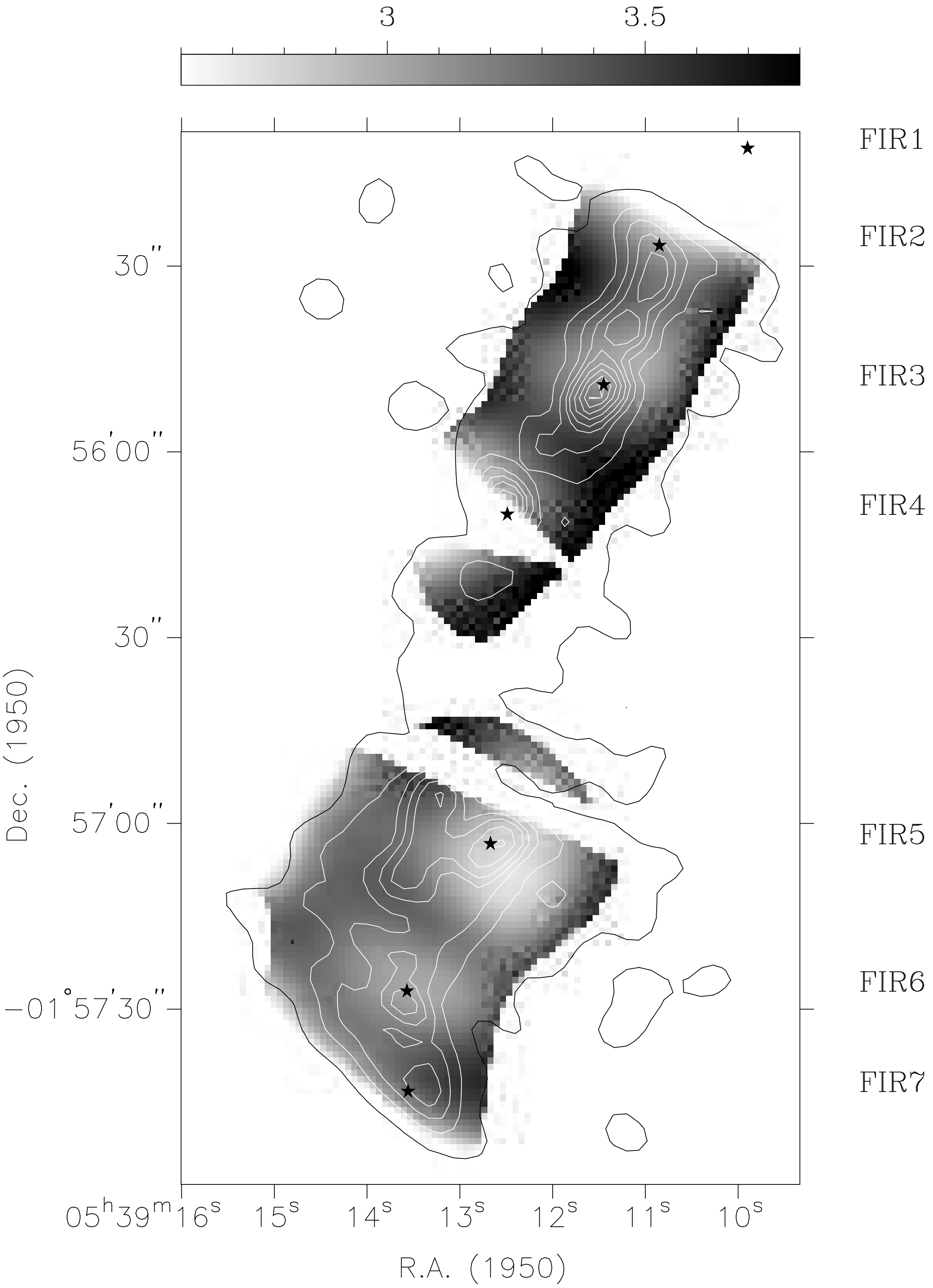

3
3.5
FIR1
FIR2
FIR3
FIR4
FIR5
FIR6
FIR7
30″
56′00″
30″
57′00″
−01°57′30″
Dec. (1950)
05h39m16s
15s
14s
13s
12s
11s
10s
R.A. (1950)

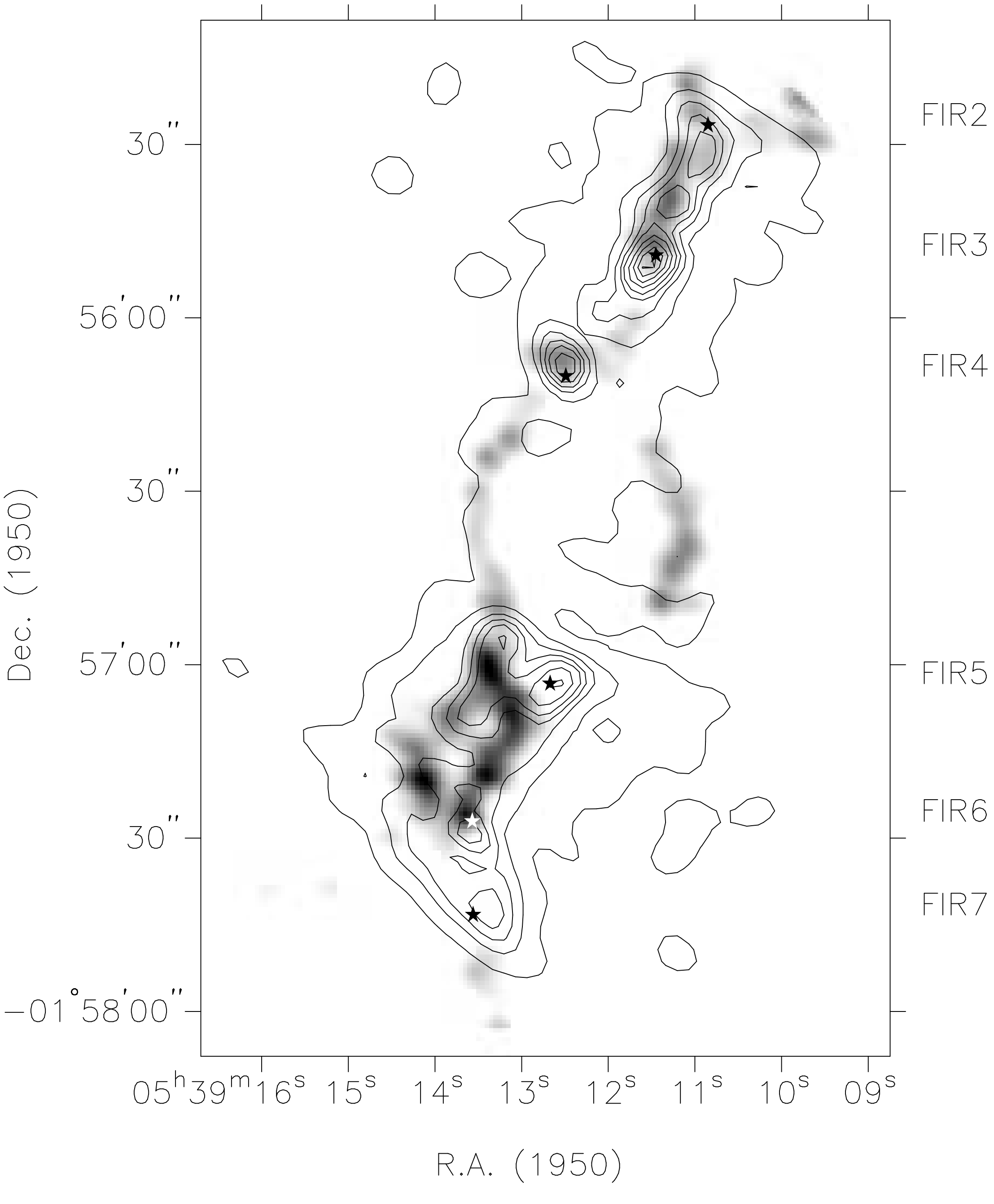
FIR2
FIR3
FIR4
FIR5
FIR6
FIR7
30″
56′00″
30″
57′00″
30″
−01°58′00″
Dec. (1950)
05h39m16s 15s 14s 13s 12s 11s 10s 09s
R.A. (1950)